# A Successive Incipient Impregnation Approach for Supporting Prussian Blue Analogues on Porous Carriers for Ammonia Adsorption

Pierre Plaza-Joly, Limor Ben Neon, Carlos Castilla-Martinez, Martin Drobek, Anne Julbe, Umit Demirci

# A Successive Incipient Impregnation Approach for Supporting Prussian Blue Analogues on Porous Carriers for Ammonia Adsorption

*Pierre Plaza-Joly, Limor Ben Neon*, Carlos Castilla Martinez, Martin Drobek*, Anne Julbe, Umit B. Demirci*

Institut Européen des Membranes (IEM); Univ Montpellier, CNRS, ENSCM, Place Eugène Bataillon; 34095 Montpellier; France

KEYWORDS: Prussian blue analogues, Porous adsorbent, Alumina, Ammonia removal, Scalable synthesis, Composite material

**ABSTRACT:**

This work presents, for the first time, the synthesis of a copper – cobalt supported Prussian Blue Analogue (PBA) on alumina porous substrates via successive incipient impregnation. This well-established method, commonly used in the preparation of metal-supported catalysts for heterogeneous catalysis, enables cost-effective, large-scale fabrication of PBAs while improving their handling. Two drying protocols, conventional and microwave drying, were investigated to assess their impact on synthesis efficiency and material properties. Notably, microwave-based drying reduced the total synthesis time to just 5 hours, making it ten times faster than conventional

one, while also enhancing crystal dispersion. The latter led to better mass transfer and diffusion during ammonia ($NH_3$) adsorption, as evidenced by higher kinetic velocity under harsh conditions (6250 ppmv). These findings demonstrate the advantage of combining successive incipient impregnation with microwave drying for the development of tailored porous PBA sorbents.

## Introduction

With the EU aiming to become climate-neutral by 2050, new energy vectors are essential for promoting sustainable energy systems [1]. Hydrogen ($H_2$) has been identified as a promising alternative to traditional fossil fuels because of its high energy density, versatility, and low environmental impact [1,2]. However, the practical deployment of hydrogen technologies faces significant challenges, particularly in $H_2$ storage, due to its low volumetric energy density (*i.e.* 0.0108 MJ/L at 1 atm and 0°C) [1]. In addition to the conventional storage methods, such as high-pressure compression and cryogenic liquefaction, reversible hydrogen storage and release via (catalytic) hydrogenation and dehydrogenation processes have attracted growing interest. In this context, solid porous materials and chemical carriers, including liquid hydrogen carriers [3,4] such as formic acid (HCOOH) [5], methanol ($CH_3OH$) [6], liquid organic hydrogen carriers (LOHCs) [7] and ammonia ($NH_3$) [8], have become key areas of primary interest.

$NH_3$ has gained particular attention due to its well-established global infrastructure and high hydrogen content (121 kg $H_2/m^3$) [8–10]. However, its conversion to hydrogen, whether via thermal catalytic cracking or electrochemical decomposition in alkaline media [9,10], remains incomplete, often leaving residual $NH_3$ in the hydrogen stream. These traces pose challenges for downstream applications, particularly in low-temperature fuel cells, where $NH_3$ contamination can degrade performance [11]. To address this issue, significant efforts are underway to develop efficient sorbent materials for hydrogen purification and, more broadly, for the removal of hazardous volatile

compounds from various gas mixtures. The main challenge is to develop sorbents that are anti-corrosive and exhibit optimal affinity toward $NH_3$.

Herein, a wide range of materials has been explored for $NH_3$ capture, each offering distinct advantages. These materials can be broadly categorized into two groups: traditional sorbents and porous framework sorbents [12]. Traditional sorbents, such as activated carbons and inorganic oxides (*e.g.,* alumina, silica), are widely used due to their availability and cost-effectiveness. However, they generally exhibit lower performance unless they are surface-modified or used as adsorbents carriers [12]. In contrast, porous framework sorbents with well-defined tunable, cage-like structure represent a more promising alternative. For instance, zeolites, which are crystalline aluminosilicates with well-ordered microporous frameworks, are highly thermally and chemically stable [13]. Their ion-exchange properties and tunable acidity make them effective for $NH_3$ adsorption, particularly under dry conditions, although their performance may decline in humid environments. Metal-Organic Frameworks (MOFs), composed of metal cations coordinated to organic ligands, offer exceptionally high surface areas and tunable pore environments, enabling strong and selective interactions with $NH_3$ molecules [14]. Some MOFs also exhibit chemisorption behavior, making them very promising for high-capacity capture [15]. Finally, Covalent Organic Frameworks (COFs), built from light elements linked by covalent bonds, have also shown potential for $NH_3$ adsorption, especially when functionalized with polar groups, acidic groups or metals [16].

Within this group of sorbents, Prussian Blue Analogues (PBAs) have emerged as promising candidates for $NH_3$ adsorption. PBAs are easy to synthesize from inexpensive chemical precursors [17]. They feature a unique open-framework structure composed of a densely organized cavity network, typically represented by the formula $AM[M'(CN)_6]$, where two transition metals (M and M') are coordinated with cyanide ($CN^-$) and an alkaline ion ($A^+$) (Figure 1). Takahashi *et al.* have

demonstrated that PBAs are effective materials for the selective capture of $NH_3$ traces [18,19]. Supporting PBAs on porous substrates enables their integration into structured sorbent systems, combining tunability with high $NH_3$ uptake potential. The existing vacancies and interstitial sites in the PBAs structure are assumed to be the primary $NH_3$ adsorption sites, although the exact nature of the interactions remains unclear [19]. Recent work by Usuda *et al.* suggests that the interaction between $NH_3$ and vacancy sites is much weaker than with interstitial sites [20]. $NH_3$ is adsorbed and coordinated at vacancy sites, whereas $NH_4^+$ ions form in interstitial sites through reaction with $H_2O$ within the PBAs framework. They observed that $NH_3$ molecules adsorbed at vacancy sites are more likely to desorb into an aqueous $NH_4HCO_3$ solution, while $NH_4^+$ ions are less prone to desorption. Additionally, the chemical nature of the metal-cyanide framework influences the interaction strength between $NH_3$ and the vacancy sites. Hence, by changing the metal centers in the PBAs structure (*e.g.* Fe-Fe, Cu-Co, Co-Fe, Cu-Fe), the affinity toward $NH_3$ can be modulated. Consequently, a library of PBAs as potential $NH_3$ sorbents with diverse physicochemical properties and structures can be developed [17].

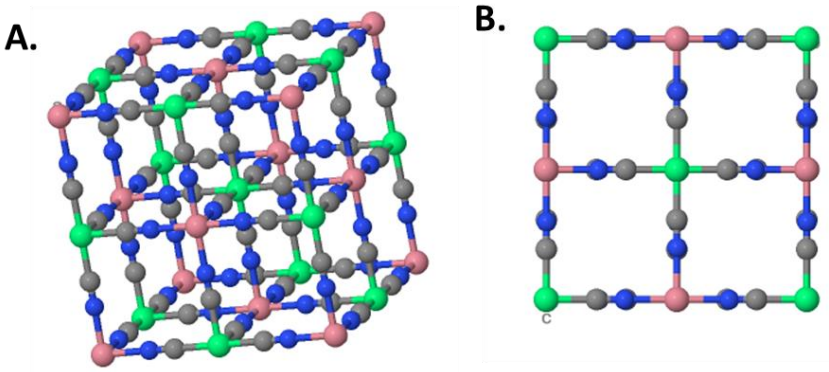


**Figure 1:** Crystal structure of a Prussian Blue analogue (PBA), $\mathbf{Cu[Co(CN)_6]_{0.66}\square_{0.33}}$. **(A)** 3D perspective view of the face-centered cubic framework showing Cu (green), Co (pink), C (gray), and N (blue) atoms. The structure consists of a cubic network of $Cu^{2+}$ and $[Co(CN)_6]^{3-}$ units

connected via cyanide bridges, with a fraction of $Co(CN)_6$ vacant sites (□), leading to structural defects. **(B)** Top-down view along the c-axis, highlighting the ordered arrangement of the metal centers and bridging cyanide ligands in the 2D projection.

Although PBAs demonstrate promising $NH_3$ adsorption capabilities, their industrial implementation faces two main challenges: *(i)* their powdery nature, which complicates handling, and *(ii)* the use of excess aqueous solutions of metal salts, leading to waste of both water and reagents. To overcome these limitations, it is increasingly important to develop straightforward synthesis methods for supporting PBAs on substrates such as pellets, beads, granules, or foams. Indeed, this approach would enable more efficient handling, along with easier regeneration and reuse [21]. Various strategies have been explored to immobilize PBAs onto solid supports, aiming to enhance their applicability in gas adsorption. Traditionally, PBAs are either deposited via dip-coating using suspensions of pre-synthesized powders [22], or synthesized *in situ* directly on the surface of selected substrates using immersion/slurry solutions or a hydrothermal cation exchange approach [23–25]. While these methods have enabled initial progress in integrating PBAs into structured and/or porous systems (*e.g.,* MOFs, $TiO_2$) [23,25], they often suffer from inherent limitations. In particular, achieving a homogeneous and stable dispersion of PBAs on macroscopic supports remains challenging. Dip-coating methods frequently results in poor adhesion and uneven coverage, whereas *in situ* growth strategies can lead to uncontrolled nucleation and aggregation, especially when applied to substrates having complex geometries. Moreover, these typical methods often require large volumes of solvents and excess metal salts to drive crystallization, raising concerns regarding scalability, cost, and environmental impact.

In this context, we propose a novel bottom-up synthesis approach for the direct growth of PBAs on alumina ceramic substrates using successive incipient impregnation. We demonstrate the

feasibility of synthesizing a copper and cobalt based PBAs on the surface of porous alumina beads while minimizing the consumption of metal-salt and solvent which is limited to the support's total pore volume. Additionally, we evaluate the impact of microwave-assisted and conventional convection drying during CuCo-PBA formation on both its final physicochemical and textural characteristics, and functional performance in $NH_3$ sorption under continuous gas flow. Our findings show that the drying procedure significantly influences the $NH_3$ sorption kinetics the CuCo-PBA by altering their crystal size. The detailed results are discussed hereafter.

## Experimental

### Materials

All reagents and materials were sourced from commercial suppliers and used as received, without further purification. Potassium hexacyanocobaltate ($K_3[Co(CN)_6]$, Sigma-Aldrich, 99%) and copper(II) nitrate hexahydrate ($Cu(NO_3)_2.6H_2O$, Sigma-Aldrich, 99%) were used to synthesize the CuCo Prussian Blue analogue (CuCo-PBA). Commercial porous alumina ($Al_2O_3$) beads (NORPRO, St-Gobain) served as the support material for CuCo-PBA deposition. These beads consist of an $\alpha$-$Al_2O_3$ porous core coated with porous $\gamma$-$Al_2O_3$. Milli-Q water (18 MΩ.cm) was used as solvent.

### Synthesis

To prepare CuCo-PBA supported on $Al_2O_3$ beads (AB), a successive incipient impregnation approach was applied (Figure 2). Briefly, a saturated impregnation solution of $Cu(NO_3).6H_2O$ was prepared to achieve a theoretical coverage of 1.65 Cu atoms per nm² on the surface of AB supports. Accordingly, for 1 g of AB ($S_{BET}$ = 126 m²/g, Vp = 0.473 cm³/g), 0.08 g of $Cu(NO_3).6H_2O$ was dissolved in 0.473 mL of Milli-Q water. The Cu solution was impregnated onto the AB, allowed to mature for 2 h, and then dried. Subsequently, a second impregnation solution containing $K_3[Co(CN)_6]$ (0.10 g in 0.473 mL of Milli-Q water) was prepared and impregnated onto the Cu-loaded AB. After 2 h of maturation, during which CuCo-PBA crystals formed on the surface, the sample was dried once more. Potassium nitrate salt formed on the surface and was subsequently removed by washing the supported CuCo-PBA with Milli-Q water under continuous agitation using a linear agitator.

To investigate the impact of the drying method applied after impregnation and washing, two approaches were employed. The first involved conventional drying, in which each drying step was performed at 80°C for 16 h. Samples prepared using this method are referred to as O-CuCo@AB. The second approach utilized microwave (MW) drying. In this case, each drying step was conducted at 700 W for 6 min using a commercial Brandt microwave oven. Samples prepared by this method are denoted as MW-CuCo@AB.

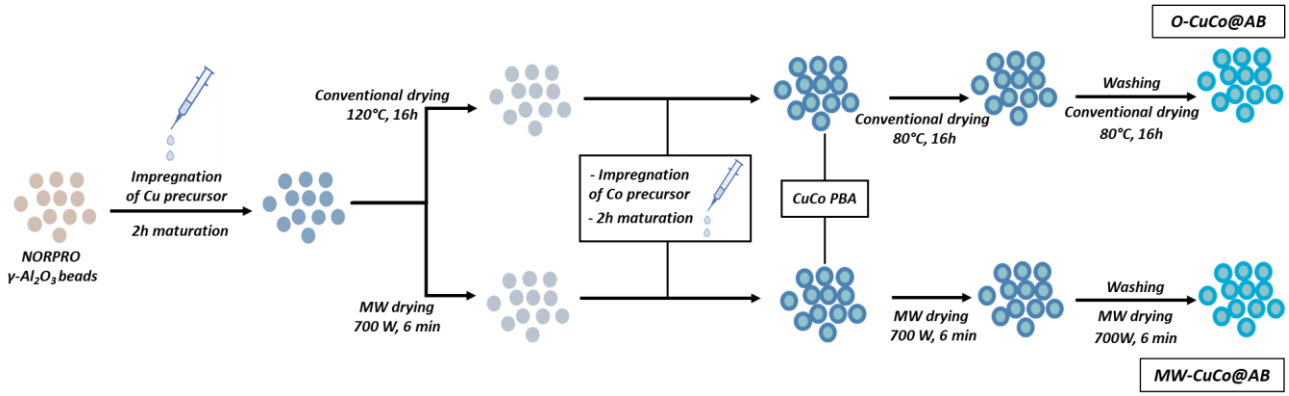


Figure 2: Schematic representation of the synthesis protocol used for preparing O-CuCo@AB and MW-CuCo@AB by successive incipient impregnation.

For comparison, unsupported CuCo-PBA powders were prepared following a protocol described elsewhere [17]. Typically, 100 mL of an aqueous solution containing $K_3[Co(CN)_6]$ (0.1 M) in Milli-Q water were added dropwise under constant stirring to an aqueous solution of $Cu(NO_3)_2.6H_2O$ (0.18 M). A blue precipitate formed immediately and was allowed to mature under constant stirring for 24 h. The resulting solid was recovered by centrifugation (Sigma 3-16P, 8000 rpm, 5 min) and washed six times with Milli-Q water.

**Physicochemical characterization**

The crystalline structure and composition of CuCo-PBA were analyzed by X-ray diffraction (XRD) and infrared attenuated total reflectance (IR-ATR) spectroscopy, respectively. XRD

measurements were performed using a PANalytical X'pert MDP-Pro diffractometer at ambient temperature, with a step size of 0.017°. The average crystallite size (D) of CuCo-PBA was calculated using the Scherrer equation. Surface morphology was analyzed using a field emission scanning electron microscope (FESEM, Hitachi S-4800). An acceleration voltage of EHT=5kV has been used. Prior to observation, samples were sputter-coated with platinum. Elemental mapping of Co, Cu, K, N, O, and C was conducted via Energy Dispersive X-ray Spectroscopy (EDX) using a Zeiss Sigma 300 SEM equipped with an Oxford Instruments X-Max N SDD detector. The elemental concentration (wt%) were determined based on the intensities of their characteristic X-ray emission energies. Quantitative elemental analysis of CuCo-PBA supported on $Al_2O_3$ beads was performed using inductively coupled plasma mass spectrometry (ICP-MS, Agilent 7900) with an automatic sample changer (Autosampler ASX-520). For ICP-MS analysis, samples were digested in nitric acid at 100 °C for 16 h. Structural and surface physicochemical analyses were carried out before and after $NH_3$ adsorption. Textural properties were evaluated by $N_2$ physisorption using a Micromeritics ASAP 2020 instrument. Prior to measurements, samples were degassed under vacuum at 150 °C. The specific surface area ($S_{BET}$) was calculated via the multipoint Brunauer–Emmett–Teller (BET) method, and the total pore volume ($V_p$) was estimated at a relative pressure ($p/p_0$) close to 0.995.

Thermogravimetric analysis (TGA) was conducted using a TA Instruments SDT Q600 and platinum crucibles as samples holders. Thermograms were recorded under a nitrogen atmosphere (100 mL/min) with a heating rate of 10 °C/min from 25 to 1000 °C.

**Adsorption measurements of $NH_3$**

Prior to $NH_3$ adsorption experiments, MW and conventionally dried supported PBA were activated under dynamic primary vacuum in a closed vessel connected to a Schlenk line and placed in an oil bath at 160 °C for 12 h. During activation, the PBA lost its bluish color and turned gray, indicating the removal of surface water. To prevent rehydration, the as-activated PBA samples were transferred into an adsorption cell inside an argon-filled glovebox.

Breakthrough curve measurements were performed to estimate the $NH_3$ adsorption capacity and evaluate adsorption kinetics using a custom-built apparatus equipped with a Perkin Elmer Clarus 400 gas chromatograph. $NH_3$ analysis was carried out using a Q-Plot column (30 m × 0.53 mm, 20 µm phase thickness). Nitrogen was used as the carrier gas at a flow rate of 15 mL/min. The oven temperature was maintained at 50 °C, and the injection temperature was set to 200 °C. For each experiment, 0.5 g of sample was used, with measurements conducted at 23 °C and 1.03 bar under a $N_2/NH_3$ gas flow mixture (61 mL/min). The $NH_3$ concentration was adjusted to 0.6 % (6250 ppm by volume, ppmv) by diluting $NH_3$ in the $N_2$ stream. This concentration ensures good measurement sensitivity (i.e., a favorable signal-to-noise ratio), thereby minimizing potential errors in the analysis. The $N_2/NH_3$ gas flow and $NH_3$ concentrations at both inlet and outlet were continuously monitored to ensure stable conditions throughout the measurements. The sorption capacities, $q_t$ (mg), at time t, were determined using the following equation:

$$q_t = Q * C_0 \int_0^t (1 - \frac{C_t}{C_0}) dt$$

where $Q$ is the volumetric flow rate (L/min), $C_0$ is the initial $NH_3$ concentration (mg/L) and $C_t$ is the concentration at time t (mg/L). To characterize the total adsorption capacity, experiments were carried out until the outlet concentration equaled the feed concentration. For comparison, pristine $Al_2O_3$ beads (AB) were tested under identical conditions to isolate the sorption capacity attributable to the supported CuCo-PBA.

Adsorption kinetics were analyzed by fitting the breakthrough curve data to a polynomial function describing concentration as a function of time. The first derivative of this fitted curve (dC/dt) was calculated to determine the instantaneous adsorption rate, with the maximum value representing the peak adsorption velocity.

## Results and discussion

As previously described, the synthesis of CuCo-PBA on ceramic substrates was accompanied by two drying protocols - conventional and microwave drying to assess their impact on synthesis efficiency and material properties. The physicochemical and functional characteristics of samples prepared using conventional drying (O-CuCo@AB) and microwave drying (MW-CuCo@AB) were evaluated and are detailed in the following paragraphs.

### Conventional drying

The successive incipient impregnation method led to the formation of CuCo-PBA structures supported on the surface of $Al_2O_3$ beads, as evidenced by SEM images (Figure 3) and PXRD patterns (Figure 4). Small, cube-shaped crystals approximately 2–3 μm in size are uniformly distributed across the support's surface. Notably, their well-defined structure is also observed within the $Al_2O_3$ beads, as shown in the cross-sectional view of O-CuCo@AB (Figure 3B). This indicates that the synthesis approach enables the diffusion of Co and Cu precursors into the porous alumina matrix, promoting CuCo-PBA formation not only on the external surface but also throughout the bulk material). Furthermore, EDX mapping confirmed that these crystallites consist of C, N, Cu, and Co- the fundamental elements constituting PBAs (Figure S1).

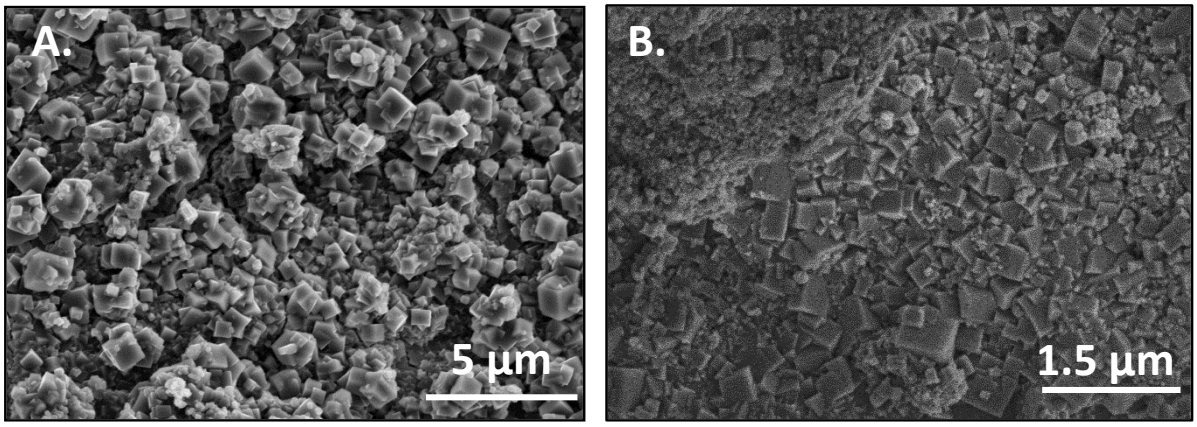


**Figure 3:** SEM images of the surface (A.) and cross-section (B.) of an O-CuCo@AB sample, showing the formation of cubic CuCo-PBA crystals on the surface and within the bulk of the support.

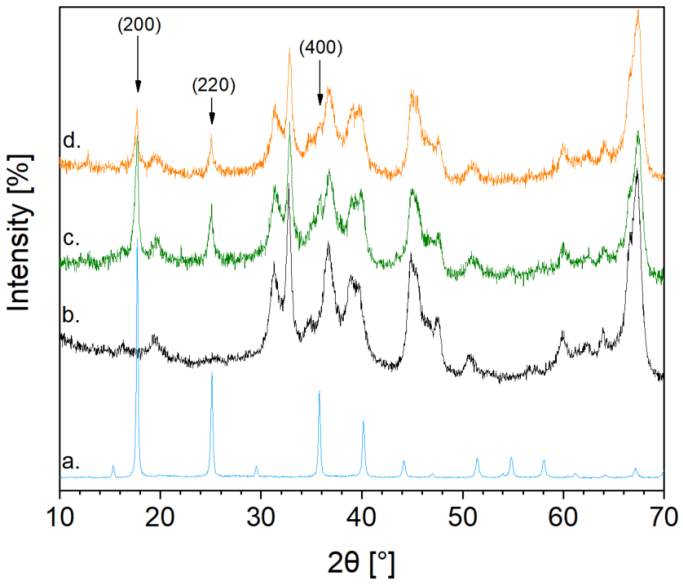


**Figure 4:** PXRD patterns of (a.) CuCo-PBA powder, (b.) pristine $Al_2O_3$ beads (AB), (c.) O-CuCo@AB, and (d.) MW-CuCo@AB.

In concordance, the PDRX pattern of O-CuCo@AB (Figure 4) confirms the formation of CuCo-PBA, as evidenced by the presence of the diffraction peaks at 17.7°, 25.1° and 35.3°, which correspond to the (200), (220) and (400) facets of the PBA structure, respectively, based on ICSD entry number 759643 [26]. Using the Scherrer equation on the Rietveld-refined PXRD pattern of O-CuCo@AB (Figure S2), the average crystallite size of the supported CuCo-PBA was determined to be approximately 32 nm (Table S1).

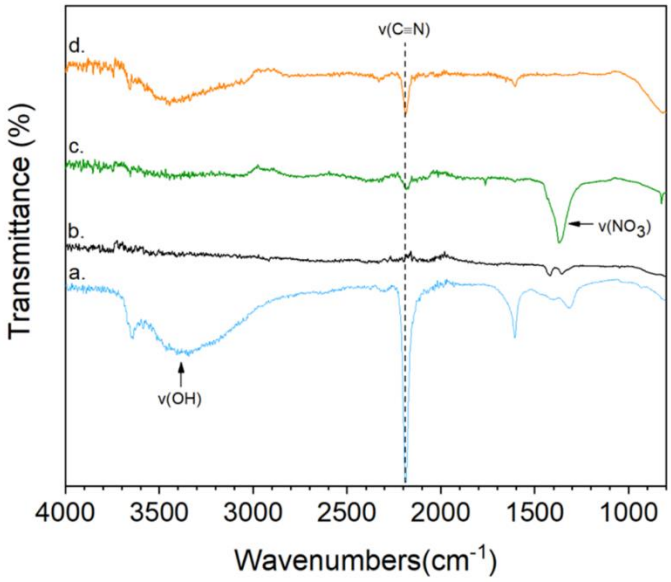


**Figure 5:** IR-ATR spectra of (a.) CuCo-PBA powder, (b.) pristine $Al_2O_3$ beads (AB), (c.) O-CuCo@AB and (d.) MW-CuCo@AB.

These crystallites are much smaller than the cubic particles observed by SEM, suggesting that the latter are aggregates of smaller crystallites forming the overall PBA cubic morphology. The inherent structural complexity of PBAs, such as framework tilts and distortions may also contribute to the polycrystalline nature of these cubic structures. The IR-ATR spectrum of O-CuCo@AB shows the characteristic absorption band of the coordinated cyanide groups from the PBA framework, observed at 2189 $cm^{-1}$ (Figure 5). Compared to unsupported CuCo-PBA, the *ν*(CN) band is less intense, likely due to the lower amount of PBA supported on $Al_2O_3$ beads.

Additionally, a moderately intense vibration band at 1362 $cm^{-1}$ is observed, ascribed to nitrate. This suggests the presence of either residual $KNO_3$ and/or non-coordinated $Cu(NO_3)_2$ precursor. Indeed, quantitative EDX and ICP-MS analyses (Table 1) confirm the presence of potassium (2 wt%), supporting the hypothesis of residual salt. However, it is also highly probable that a portion of the detected $K^+$ is caged within the PBA structure, making it more difficult to remove during the applied one-hour washing step. Besides, EDX mapping revealed an uneven distribution of Cu and Co atoms across the $Al_2O_3$ surface (Figure S3). Certain regions exhibited lower concentrations of both metals, limiting the formation of CuCo-PBA in these areas. Overall, based on ICP-MS measurements and assuming that the total amount of Co and Cu precursors formed PBA with the formula $Cu(Co(CN)_6)_{0.66}\square_{0.33}$, an estimated 5 wt% of CuCo-PBA was directly formed on the AB support via successive incipient impregnation.

**Table 1:** Average weight percent concentrations of C, N, Cu, Co, and K atoms, as evaluated by EDX, for O-CuCo@AB and MW-CuCo@AB. The quantified amounts (wt%) of Cu, Co and K were determined via ICP-MS for both samples. Cu/Co weight ratios and the theoretical loading of CuCo-PBA on $Al_2O_3$ supports were calculated based on the chemical formula $Cu[Co(CN)_6]_{0.66}\square_{0.33}$, where □ denotes a lacunar site.

| *Sample* | *[Cu] wt%* | *[Co] wt%* | *[C] wt%* | *[N] wt%* | *[K] wt%* | *Cu/Co mass ratio* | *[CuCo-PBA] on $Al_2O_3$ beads, wt%* |
|---|---|---|---|---|---|---|---|
| **EDX** | | | | | | | |
| O-CuCo@AB | 8.1 ± 5.9 | 1.45 ± 0.6 | 31.3 ± 7.7 | 16.2 ± 10.2 | 0.5 ± 0.2 | - | - |
| MW-CuCo@AB | 8.4 ± 2.2 | 4.7 ± 1.5 | 40.0 ± 8.3 | 11.1 ± 5.9 | 0.2 ± 0.1 | - | - |
| **ICP-MS (RSD 1%)** | | | | | | | |
| O-CuCo@AB | 1.8 | 0.9 | - | - | 2.1 | 1.9 | 5.1 |
| MW-CuCo@AB | 1.4 | 0.7 | - | - | 1.3 | 1.9 | 3.9 |

$N_2$ sorption isotherms revealed $S_{BET}$ and pore volume of 110 $m^2/g$ and 0.36 $cm^3/g$, respectively, for O-CuCo@AB. These values indicate that the as-synthesized supported sorbent possesses suitable porosity for adsorption applications (Table 2). However, when comparing this $S_{BET}$ area to one of pristine $Al_2O_3$ support, an unexpected decrease of 13 % is noted for O-CuCo@AB. Given that O-CuCo@AB contains approximately 5 wt% of CuCo-PBA, a theoretical surface area of about 170 $m^2/g$ would be expected - calculated using the equation: 0.05 x $S_{BET}$ (CuCo-PBA) + 0.95 x $S_{BET}$ (AB). This discrepancy could be related to the partial pore clogging of alumina pores by the formation of CuCo-PBA and presumably $KNO_3$ salt. Two observations support this hypothesis: (i) the AB support has sufficiently large pores, (~ 10 nm in diameter), which can accommodate the formation of PBA crystals within its structure; (ii) a significant reduction in specific surface area (down to 75 $m^2/g$) was observed for O-CuCo@AB samples that were not subjected to the washing step (Figure S4).

**Table 2:** Textural analysis results of O-CuCo@AB and MW-CuCo@AB samples. An estimated error of ~10% is associated with the values of specific surface area ($S_{BET}$) and pore volume ($V_p$).

| *Sample* | *$S_{BET}$ ($m^2/g$)* | *Vp ($cm^3/g$)* |
|---|---|---|
| O-CuCo@AB | 110 | 0.36 |
| MW-CuCo@AB | 94 | 0.32 |
| $Al_2O_3$ beads (AB support) | 126 | 0.47 |
| CuCo-PBA powder (not supported) | 1011 | 0.95 |

**Microwave drying**

MW drying was explored as a means to reduce the time and energy consumption associated with prolonged conventional drying at elevated temperatures. This approach shortened the overall

synthesis duration from three days to less than 5 hours. Importantly, MW drying did not prevent the formation of CuCo-PBA on alumina beads, as evidenced on the MW-CuCo@AB sample. Similar to O-CuCo@AB, the three characteristic diffraction peaks of PBA were detected by PXRD, and the $\nu$(CN) band appeared at 2189 $cm^{-1}$ in the IR-ATR spectrum. Using the Scherrer equation, an average crystallite size of 30 nm was calculated (Figure S5), comparable to that of the conventionally dried sample, indicating that the drying method had no significant impact on crystallite size. However, SEM images revealed smaller PBA crystals (< 1 µm) uniformly dispersed across the surface for the MW-dried sample (Figure 6). This observation aligns with literature reports demonstrating that MW drying enhances metal dispersion after impregnation [27]. During drying, MW irradiation is absorbed by the matter, generating numerous localized hotspots on the solid surface. This promotes more homogenous and rapid water evaporation, favoring the formation of smaller crystallite aggregates and well-dispersed CuCo-PBA crystals. Due to this physical effect, local surface temperatures exceeding 80 °C can be reached - higher than those typically achieved with convectional drying. This also explains the absence of $\nu(NO_3)$ band on the IR-ATR spectrum (Figure 4b).

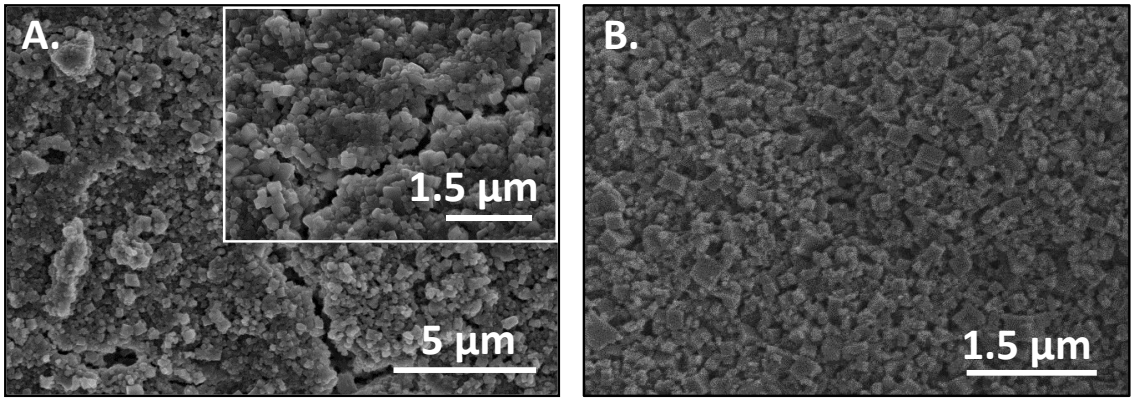


**Figure 6:** SEM images of (A.) the surface of MW-CuCo@AB and (B.) a cross-section view of MW-CuCo@AB.

Although MW drying affected the crystal size of CuCo-PBA, it did not influence the specific surface area ($S_{BET}$). In fact, surfaces areas and pore volumes comparable to those of conventionally dried samples were measured, with a similar trend of partially clogged pores and reduced specific surface area (Table 2).

EDX and ICP-MS analyses indicate that the elemental composition of MW-CuCo@AB is comparable to the one of O-CuCo@AB (Table 1). Despite the thorough washing step after PBA synthesis, a small but detectable amount of potassium remains. As previously discussed, potassium located inside the PBA cages is more difficult to remove, which might explain its persistence. Based on ICP-MS results and assuming that the total amount of loaded Co and Cu was converted into CuCo-PBA, estimated CuCo-PBA content of ~4 wt% was determined in MW-CuCo@AB samples.

**$NH_3$ breakthrough measurements**

To evaluate the s $NH_3$ sorption performance of the supported CuCo-PBA samples (MW-CuCo@AB and O-CuCo@AB), $NH_3$ breakthrough curve measurements were carried out under a continuous $N_2/NH_3$ gas flow (6250 ppmv, 61 mL/min). This elevated concentration was deliberately chosen to (i) evaluate the material's stability under harsh operating conditions and (ii) asses its potential applicability in environmental or industrial contexts where high ammonia levels may pose operational or safety concerns. The dynamic behavior of $NH_3$ capture in the gas stream was analyzed in terms of both sorption capacity and kinetics (Figure 7).

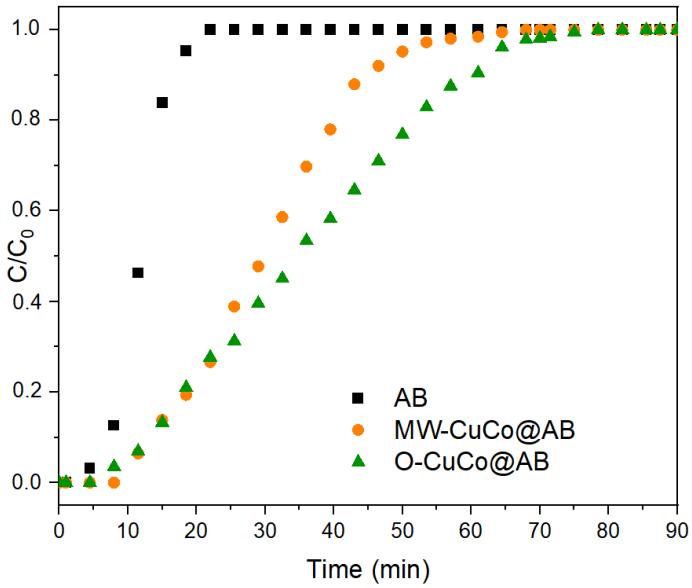


**Figure 7:** $NH_3$ breakthrough curves for pristine $Al_2O_3$ beads (AB), MW-CuCo@AB, and O-CuCo@AB composite materials, measured at room temperature with a gas flow rate of 61 mL/min and a $NH_3$ concentration of 6250 ppmv.

**Sorption capacity of supported CuCo-PBA**

The $NH_3$ breakthrough curves show distinct behaviors. The pristine $Al_2O_3$ support reached saturation rapidly, whereas both CuCo@AB samples exhibited S-shaped curves, indicating longer saturation times. Under the selected experimental conditions, the pristine $Al_2O_3$ support became fully saturated after 22 min, whereas MW-CuCo@AB and O-CuCo@AB reached saturation after 68 min and 75 min, respectively. These results indicate that both CuCo@AB samples have higher sorption capacities than the pristine support.

As reported in Table 3, the $NH_3$ sorption capacities for O-CuCo@AB and MW-CuCo@AB are 17.1 $mg_{NH3}/g$ and 14.5 $mg_{NH3}/g$, respectively. Based on the estimated amount of CuCo-PBA formed in the supported samples, the individual contributions of the alumina support and the PBA to the overall $NH_3$ sorption capacity can be determined (Table 3). It is noteworthy that the alumina

support contributes minimally to $NH_3$ adsorption, with a capacity of 6.5 $mg_{NH3}/g$. In contrast, as expected, CuCo-PBA samples exhibit a much stronger affinity for ammonia, with sorption capacities around 200 $mg_{NH3}/g_{PBA}$. These values are consistent with the sorption capacity of pristine CuCo-PBA powder (231 $mg_{NH3}/g$), indicating that neither the deposition method nor the drying method significantly affects the performance of supported CuCo-PBA. This finding underscores the potential of successive incipient impregnation as a scalable method for manufacturing high performance supported PBAs.

**Table 3:** Comparison of $NH_3$ sorption capacities for MW-CuCo@AB and O-CuCo@AB$_3$, the $Al_2O_3$ support (AB), and CuCo-PBA powder. For normalizing sorption capacities, the amount of Cu, Co and K were quantified via ICP-MS analysis considering $Cu[Co(CN)_6]_{0.66}\square_{0.33}$ (with □ indicating a lacuna of the PBA).

| *Sorbent sample* | *Sorption capacity of the material* ($mg_{NH3}/g_{sorbent}$) | *Sorption capacity Excluding support contribution* ($mg_{NH3}/g_{sorbent}$) | *Sorption capacity of PBA and normalized sorption capacity reported to the amount of PBA in CuCo@AB* ($mg_{NH3}/g_{PBA}$) |
|---|---|---|---|
| O-CuCo@AB | 17.1 | 10.6 | 206 |
| MW-CuCo@AB | 14.5 | 8.0 | 202 |
| Pristine $Al_2O_3$ beads (AB) | 6.5 | - | - |
| CuCo-PBA powder | - | - | 231 |

It should be emphasized that the sorption capacities determined for supported CuCo-PBA are estimated under the assumption that the total amount of Co and Cu precursors is fully converted into PBA, and that all adsorption sites are unoccupied after evacuation. However, as previously discussed, a relatively significant amount of potassium (1-2 wt%) was detected by ICP-MS despite thorough washing, suggesting the presence of caged $K^+$ ions in interstitial sites [28]. As a result, a portion of the potential $NH_3$ adsorption sites is likely blocked by $K^+$, thereby inhibiting $NH_3$ uptake, as already demonstrated in other works [29,30]. Consequently, the sorption capacities reported for CuCo-PBA are likely slightly overestimated.

When comparing the $NH_3$ sorption capacity of the supported PBAs with values reported in the literature (Table 4), it is noteworthy that the synthesized PBAs exhibit similar capacities as Fe-PBA and CuFe-PBA, despite being tested at higher $NH_3$ concentrations. This is of particular interest, as the CuCo-PBA synthesized in this work achieves high sorption capacities (up to 200

$mg_{NH3}/g_{PBA}$) under harsh conditions (6250 ppmv $NH_3$ under $N_2$ flow). TGA carried out directly on samples upon $NH_3$ adsorption (Figure S6) revealed two distinct $NH_3$ desorption events: a first peak at 86 °C and a second at 235 °C, corresponding to physisorbed and coordinated $NH_3$, respectively [31]. In overall, the $NH_3$ loss accounted for 22 wt%, equivalent to 220 $mg_{NH3}/g_{sample}$, which aligns well with the sorption capacity determined for CuCo@AB.

**Table 4:** Comparison of $NH_3$ sorption capacities reported in the literature for different PBAs.

| *Material* | *Capacity (mg/g)* | *$NH_3$ Concentration (ppm)* | *Flow Rate* | *Reference* |
|---|---|---|---|---|
| Supported CuCo-PBA | 200 | 6250 ppmv | 61 mL/min | This work |
| CuCo-PBA powder | 231 | | | |
| Fe-PBA | 211 | 0.015–1.0 | 500 mL/min | [19] |
| CuFe-PBA | 225 | 3680 | static | [20] |
| Co-PBA | 83 | | | |
| CoFe-PBA | 25 | | | |

**Sorption kinetics**

The profile of the $NH_3$ breakthrough curves varies depending on the applied drying method. Specifically, the slope of the curve for MW-CuCo@AB is steeper than that of O-CuCo@AB. Maximum kinetic velocities during breakthrough were determined to be 0.0904 $min^{-1}$ for MW-CuCo@AB and 0.0313 $min^{-1}$ for O-CuCo@AB (Figures S7 and S8). This indicates that mass transfer during $NH_3$ sorption is 3 times faster for the MW-dried samples than for the conventionally dried ones. This significant difference can be attributed to two main factors. First, SEM images reveal much smaller CuCo-PBA crystals in the MW-dried sample, resulting in larger contact surface area and shorter diffusion paths within the PBA crystal network. Second, EDX-mapping

shows the presence of isolated Co, Cu, and Al sites (i.e., regions without PBA), which are directly accessible and may adsorb $NH_3$ more rapidly. The quantities of these sites may differ between MW- and conventionally dried samples, slightly influencing the sorption kinetics.

It should be noted that despite the promising $NH_3$ sorption capacities and kinetics for applications where minimizing pressure drop in PBA-based sorbent columns is critical, the chemical stability of PBA remains a significant concern. Experimental exposure to very high concentrations of ammonia (6250 ppmv, as tested in this study) has shown that the structural integrity of the material may be compromised. While this does not pose an important problem for trace ammonia removal at low concentrations, it could present challenges for long-term use or in scenarios involving occasional exposure to high concentration peaks. This issue could be partially mitigated by employing alternative PBAs with different metal centers, which may offer improved chemical stability for application conducted in harsh conditions.

## Conclusion

In this work, we demonstrate for the first time that successive incipient impregnation is an efficient and rapid method for synthesizing supported PBAs. This approach, commonly used in heterogeneous catalysis, enables scalable production of supported PBAs while minimizing solvent usage and energy consumption, particularly when combined with microwave (MW) drying.

Both conventional and MW drying methods yield PBAs with comparable structural and textural properties. However, a key distinction lies in particle size. The use of MW irradiation during the drying step favors the formation of smaller PBA particles (<1 μm), attributed to more uniform surface heating and the creation of localized hotspots that accelerate water evaporation. This rapid drying suppresses crystallite aggregation, leading to better dispersion of the sorbent phase. As a result, the enhanced dispersion of CuCo-PBA on alumina beads enabled to a threefold increase in $NH_3$ adsorption kinetics, reflecting improved diffusion and mass transfer.

A critical drawback of the material lies in its limited stability upon exposure to ammonia at high concentration (6250 ppmv tested in this work to simulate harsh conditions), highlighting a major challenge for long-term application. In a broader context, stability issues could be addressed by applying the strategy developed in this work to other types of PBAs with different metal-metal combinations (e.g., CoCo, CuFe and CoFe).

In a wider context, the synthesis approach developed in this study paves the way for broader application of supported PBAs, not only as sorbents for hazardous compounds but also in (electro)catalysis, by enabling their direct synthesis on other porous supports, including conductive carbon-based materials (*e.g.,* carbon black, graphene) and metal oxides.

## ASSOCIATED CONTENT

AUTHOR INFORMATION


### Corresponding Author

* Martin Drobek - Institut Européen des Membranes, UMR 5635, Université de Montpellier, ENSCM, CNRS, Place Eugène Bataillon, F-34095 Montpellier cedex 5, France

Email: martin.drobek@umontpellier.fr

* Limor Ben Neon - Institut Européen des Membranes, UMR 5635, Université de Montpellier, ENSCM, CNRS, Place Eugène Bataillon, F-34095 Montpellier cedex 5, France

Email: limor.ben-neon@umontpellier.fr


### Author Contributions

Conceptualization, L.B.N., P.P.J.; Methodology, L.B.N., P.P.J.

Investigation, P.P.J., L.B.N., M.D., C.A.C.M.; Data curation, P.P.J., L.B.N.;

Writing - original draft preparation, P.P.J., L.B.N.; Review and editing, L.B.N., M.D., C.A.C.M., U.B.D., and A.J.;

Supervision, project administration and funding acquisition, M.D., U.B.D., and A.J.

All authors have read and agreed on the published version of the manuscript. The authors declare that they have no known competing financial interests or personal relationships that could have appeared to influence the work reported in this paper.


### Funding Sources

The authors gratefully acknowledge the Doctoral School Chimie Balard (ED459) for awarding a PhD fellowship to P.P.J. The authors also thank La Région Occitanie for funding the $NH_3$ adsorption setup (READYNOV 2022 call; HEAD'OCC project).

**Notes**

The authors declare no competing financial interest. The funders had no role in the design of the study; in the collection, analyses, or interpretation of data; in the writing of the manuscript; or in the decision to publish the results. The authors used GenIA (ChatGPT) to improve the language and the readability of our manuscript.

**SUPPORTING INFORMATION**

Figure S1-S8: Figure S1. EDX mapping of O-CuCo@AB. Figure S2. Rietveld refinement for O-CuCo@AB. Figure S3. Large scale EDX mapping of O-CuCo@AB. Figure S4. $N_2$ adsorption/desorption isotherms for unwashed O-CuCo@AB. Figure S5. Rietveld refinement for MW-CuCo@AB. Figure S6. TGA analysis of O-CuCo@AB after $NH_3$ sorption. Figure S7. Curve fitting of the $NH_3$ breakthrough curve of MW-CuCo@AB. Figure S8. Curve fitting of the $NH_3$ breakthrough curve of O-CuCo@AB. Table S1: Lattice parameter and crystallite size of unsupported and both supported PBA beads.

**ACKNOWLEDGMENT**

Bertrand Rebiere and Bernard Fraisse (UAR Plateforme d'Analyses et Caractérisations Chimie Balard Montpellier, Univ Montpellier, CNRS, ENSCM) are acknowledged for SEM-EDX and XRD analyses, respectively. We also thank Christophe Charmette and Jim Cartier (Institut

Européen des Membranes, CNRS) for their supports with $NH_3$ adsorption tests. Special thanks are extended to Saint-Gobain for providing the alumina supports.

## REFERENCES


(1) Van Greevenbroek, K.; Schmidt, J.; Zeyringer, M.; Horsch, A. Little to Lose: The Case for a Robust European Green Hydrogen Strategy. *Joule* **2024**, 101974. https://doi.org/10.1016/j.joule.2025.101974.

(2) Abdin, Z.; Zafaranloo, A.; Rafiee, A.; Mérida, W.; Lipiński, W.; Khalilpour, K. R. Hydrogen as an Energy Vector. *Renew. Sustain. Energy Rev.* **2020**, *120* (December 2019). https://doi.org/10.1016/j.rser.2019.109620.

(3) Elberry, A. M.; Thakur, J.; Santasalo-Aarnio, A.; Larmi, M. Large-Scale Compressed Hydrogen Storage as Part of Renewable Electricity Storage Systems. *Int. J. Hydrogen Energy* **2021**, *46* (29), 15671–15690. https://doi.org/10.1016/j.ijhydene.2021.02.080.

(4) Faye, O.; Szpunar, J.; Eduok, U. A Critical Review on the Current Technologies for the Generation, Storage, and Transportation of Hydrogen. *Int. J. Hydrogen Energy* **2022**, *47* (29), 13771–13802. https://doi.org/10.1016/j.ijhydene.2022.02.112.

(5) Eppinger, J.; Huang, K. W. Formic Acid as a Hydrogen Energy Carrier. *ACS Energy Lett.* **2017**, *2* (1), 188–195. https://doi.org/10.1021/acsenergylett.6b00574.

(6) Garg, N.; Sarkar, A.; Sundararaju, B. Recent Developments on Methanol as Liquid Organic Hydrogen Carrier in Transfer Hydrogenation Reactions. *Coord. Chem. Rev.* **2021**, *433*, 213728. https://doi.org/10.1016/j.ccr.2020.213728.

(7) Preuster, P.; Papp, C.; Wasserscheid, P. Liquid Organic Hydrogen Carriers (LOHCs): Toward a Hydrogen-Free Hydrogen Economy. *Acc. Chem. Res.* **2017**, *50* (1), 74–85. https://doi.org/10.1021/acs.accounts.6b00474.

(8) Miyaoka, H.; Miyaoka, H.; Ichikawa, T.; Ichikawa, T.; Kojima, Y. Highly Purified Hydrogen Production from Ammonia for PEM Fuel Cell. *Int. J. Hydrogen Energy* **2018**, *43*

(31), 14486–14492. https://doi.org/10.1016/j.ijhydene.2018.06.065.

(9) Spatolisano, E.; Pellegrini, L. A.; de Angelis, A. R.; Cattaneo, S.; Roccaro, E. Ammonia as a Carbon-Free Energy Carrier: NH3 Cracking to H2. *Ind. Eng. Chem. Res.* **2023**, *62* (28), 10813–10827. https://doi.org/10.1021/acs.iecr.3c01419.

(10) Lucentini, I.; Garcia, X.; Vendrell, X.; Llorca, J. Review of the Decomposition of Ammonia to Generate Hydrogen. *Ind. Eng. Chem. Res.* **2021**, *60* (51), 18560–18611. https://doi.org/10.1021/acs.iecr.1c00843.

(11) Jeerh, G.; Zhang, M.; Tao, S. Recent Progress in Ammonia Fuel Cells and Their Potential Applications. *J. Mater. Chem. A* **2021**, *9* (2), 727–752. https://doi.org/10.1039/d0ta08810b.

(12) Han, B.; Butterly, C.; Zhang, W.; He, J. zheng; Chen, D. Adsorbent Materials for Ammonium and Ammonia Removal: A Review. *J. Clean. Prod.* **2021**, *283*, 124611. https://doi.org/10.1016/j.jclepro.2020.124611.

(13) Helminen, J.; Helenius, J.; Paatero, E.; Turunen, I. Adsorption Equilibria of Ammonia Gas on Inorganic and Organic Sorbents at 298.15 K. *J. Chem. Eng. Data* **2001**, *46* (2), 391–399. https://doi.org/10.1021/je000273+.

(14) Lu, W.; De Alwis Jayasinghe, D.; Schröder, M.; Yang, S. Ammonia Storage in Metal-Organic Framework Materials: Recent Developments in Design and Characterization. *Accounts Mater. Res.* **2024**, *5*, 1279–1290. https://doi.org/10.1021/accountsmr.4c00183.

(15) Guo, L.; Han, X.; Ma, Y.; Li, J.; Lu, W.; Li, W.; Lee, D.; da Silva, I.; Cheng, Y.; Rudić, S.; Manuel, P.; Frogley, M. D.; Ramirez-Cuesta, A. J.; Schröder, M.; Yang, S. High Capacity Ammonia Adsorption in a Robust Metal-Organic Framework Mediated by Reversible Host-Guest Interactions. *Chem. Commun.* **2022**, *300*, 5753–5756. https://doi.org/10.1039/d2cc01197b.

(16) Yang, Y.; Faheem, M.; Wang, L.; Meng, Q.; Sha, H.; Yang, N.; Yuan, Y.; Zhu, G. Surface Pore Engineering of Covalent Organic Frameworks for Ammonia Capture through Synergistic Multivariate and Open Metal Site Approaches. *ACS Cent. Sci.* **2018**, *4* (6), 748–754. https://doi.org/10.1021/acscentsci.8b00232.

(17) Boudjema, L.; Mamontova, E.; Long, J.; Larionova, J.; Guari, Y.; Trens, P. Prussian Blue Analogues for the Separation of Hydrocarbons in Humid Conditions. *Inorg. Chem.* **2017**, *56* (14), 7598–7601. https://doi.org/10.1021/acs.inorgchem.7b00563.

(18) Takahashi, A.; Minami, K.; Noda, K.; Sakurai, K.; Kawamoto, T. Trace Ammonia Removal from Air by Selective Adsorbents Reusable with Water. *ACS Appl. Mater. Interfaces* **2020**, *12* (13), 15115–15119. https://doi.org/10.1021/acsami.9b22384.

(19) Takahashi, A.; Tanaka, H.; Parajuli, D.; Nakamura, T.; Minami, K.; Sugiyama, Y.; Hakuta, Y.; Ohkoshi, S. I.; Kawamoto, T. Historical Pigment Exhibiting Ammonia Gas Capture beyond Standard Adsorbents with Adsorption Sites of Two Kinds. *J. Am. Chem. Soc.* **2016**, *138* (20), 6376–6379. https://doi.org/10.1021/jacs.6b02721.

(20) Usuda, H.; Mishima, Y.; Kawamoto, T.; Minami, K. Desorption of Ammonia Adsorbed on Prussian Blue Analogs by Washing with Saturated Ammonium Hydrogen Carbonate Solution. *Molecules* **2022**, *27* (24). https://doi.org/10.3390/molecules27248840.

(21) Minami, K.; Takahashi, A.; Sakurai, K.; Mikasa, H.; Takasaki, M.; Doshu, N.; Aoyama, K.; Nakamura, T.; Iwai, R.; Kawamoto, T. Apparatus for Ammonia Removal in Livestock Farms Based on Copper Hexacyanoferrate Granules. *Biosyst. Eng.* **2022**, *216*, 98–107. https://doi.org/10.1016/j.biosystemseng.2022.02.002.

(22) Wang, S.; Cai, J.; Lv, C.; Hu, C.; Guan, H.; Wang, J.; Shi, Y.; Song, J.; Watanabe, A.; Ge, X. General and Scalable Preparation of Prussian Blue Analogues on Arbitrary Conductive

Substrates and Their Derived Metal Phosphides as Highly Efficient and Ultra-Long-Life Bifunctional Electrocatalysts for Overall Water Splitting. *Chem. Eng. J.* **2021**, *420* (129972). https://doi.org/10.1016/j.cej.2021.129972.

(23) Xiao, X.; Zhang, G.; Xu, Y.; Zhang, H.; Guo, X.; Liu, Y.; Pang, H. A New Strategy for the Controllable Growth of MOF@PBA Architectures. *J. Mater. Chem. A* **2019**, *7* (29), 17266–17271. https://doi.org/10.1039/c9ta05409j.

(24) Ai, S.; Guo, X.; Zhao, L.; Yang, D.; Ding, H. Zeolitic Imidazolate Framework-Supported Prussian Blue Analogues as an Efficient Fenton-like Catalyst for Activation of Peroxymonosulfate. *Colloids Surfaces A Physicochem. Eng. Asp.* **2019**, *581*, 123796. https://doi.org/10.1016/j.colsurfa.2019.123796.

(25) Feng, L.; Li, N.; Tang, S.; Guo, Y.; Zheng, J.; Li, X. Photoelectrochemical Performance of Titanium Dioxide/Prussian Blue Analogue Synthesized by Impregnation Conversion Method as Photoanode. *Inorg. Chem. Commun.* **2021**, *125*, 108349. https://doi.org/10.1016/j.inoche.2020.108349.

(26) Boström, H. L. B.; Collings, I. E.; Cairns, A. B.; Romao, C. P.; Goodwin, A. L. High-Pressure Behaviour of Prussian Blue Analogues: Interplay of Hydration, Jahn-Teller Distortions and Vacancies. *Dalt. Trans.* **2019**, *48* (5), 1647–1655. https://doi.org/10.1039/c8dt04463e.

(27) Auvray, X.; Thuault, A. Effect of Microwave Drying, Calcination and Aging of Pt/Al2O3 on Platinum Dispersion. *Catalysts* **2018**, *8* (9), 1–8. https://doi.org/10.3390/catal8090348.

(28) Asakura, D.; Okubo, M.; Mizuno, Y.; Kudo, T.; Zhou, H.; Ikedo, K.; Mizokawa, T.; Okazawa, A.; Kojima, N. Fabrication of a Cyanide-Bridged Coordination Polymer Electrode for Enhanced Electrochemical Ion Storage Ability. *J. Phys. Chem. C* **2012**, *116*

(15), 8364–8369. https://doi.org/10.1021/jp2118949.

(29) Kang, S.; Lee, B.; Ahn, K. H.; Im, S.; Kim, B.; Kim, T. H.; Hwang, Y.; Chae, S. Facile Synthesis of Copper-Substituted Prussian Blue Analog Immobilized Ion Exchange Resins for High-Performance Ammonium Recovery from Wastewater: Adsorption Kinetics, Isotherms, and Regeneration. *Chem. Eng. J.* **2023**, *457* (October 2022), 141128. https://doi.org/10.1016/j.cej.2022.141128.

(30) Fang, Q.; Zhu, B.; Sun, Y.; Song, W.; Xu, M. Effects of Alkali Metal Poisoning and Cobalt Modification on the NH3 Adsorption Behavior on the MnxOy/Ni (1 1 1) Surface: A DFT-D Study. *Appl. Surf. Sci.* **2020**, *509* (December 2019), 144901. https://doi.org/10.1016/j.apsusc.2019.144901.

(31) Li, W. J.; Han, C.; Cheng, G.; Chou, S. L.; Liu, H. K.; Dou, S. X. Chemical Properties, Structural Properties, and Energy Storage Applications of Prussian Blue Analogues. *Small* **2019**, *15* (32), 1–21. https://doi.org/10.1002/smll.201900470.

**TOC**

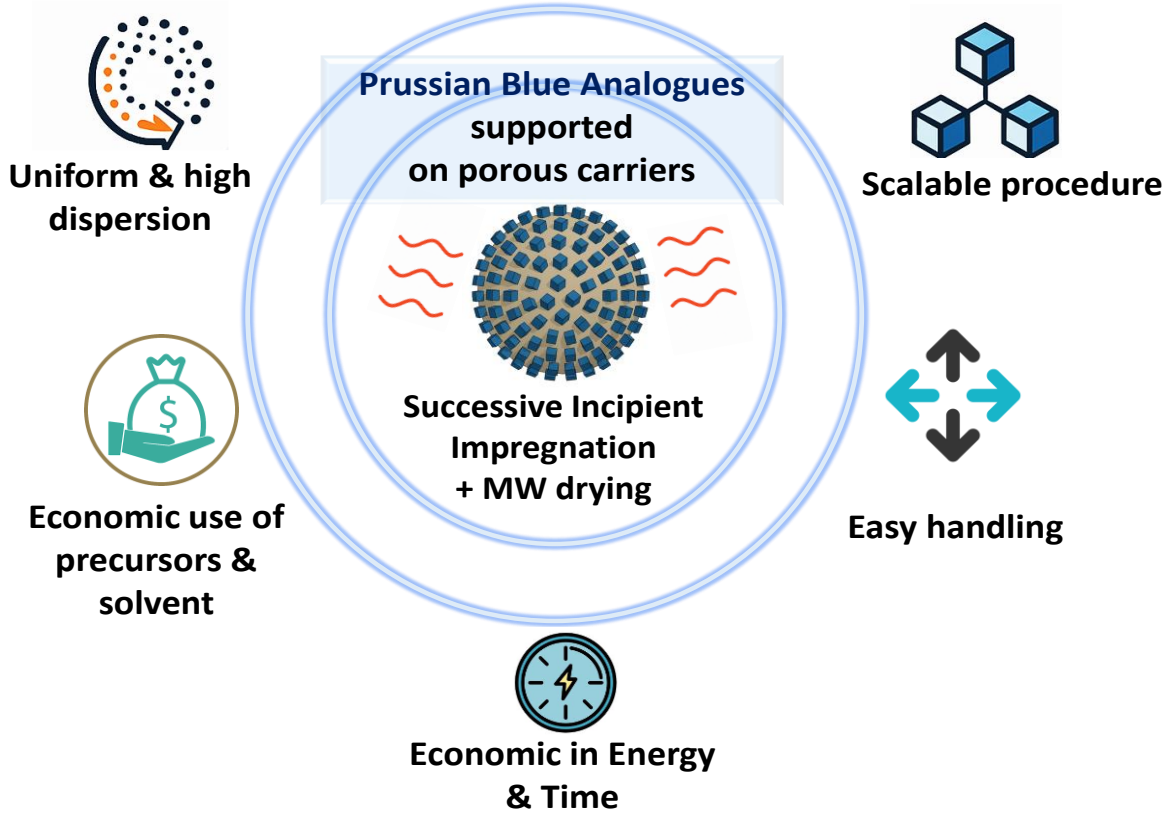
Prussian Blue Analogues
supported
on porous carriers
Uniform & high dispersion
Scalable procedure
Successive Incipient Impregnation + MW drying
Economic use of precursors & solvent
Easy handling
Economic in Energy & Time